The Astronomical Journal, 154:126 (9pp), 2017 September https://doi.org/10.3847/1538-3881/aa8450

Observations of the Ultraviolet-bright Star Y453 in the Globular Cluster M4 (NGC 6121)

William V. Dixon[1], Pierre Chayer[1], Marilyn Latour[2], Marcelo Miguel Miller Bertolami[3], and Robert A. Benjamin[4]
[1] Space Telescope Science Institute, 3700 San Martin Drive, Baltimore, MD 21218, USA; dixon@stsci.edu
[2] Dr. Karl Remeis-Observatory & ECAP, Astronomical Institute, Friedrich-Alexander University Erlangen-Nuremberg, Sternwartstr. 7, D-96049 Bamberg, Germany
[3] Instituto de Astrofísica de La Plata, UNLP-CONICET, Paseo del Bosque s/n, 1900 La Plata, Argentina
[4] Department of Physics, University of Wisconsin-Whitewater, 800 West Main Street, Whitewater, WI 53190, USA
Received 2017 May 19; revised 2017 August 2; accepted 2017 August 2; published 2017 August 31

Abstract

We present a spectral analysis of the UV-bright star Y453 in M4. Model fits to the star's optical spectrum yield $T_{\rm eff} \sim 56{,}000$ K. Fits to the star's FUV spectrum, obtained with the Cosmic Origins Spectrograph on board the *Hubble Space Telescope*, reveal it to be considerably hotter, with $T_{\rm eff} \sim 72{,}000$ K. We adopt $T_{\rm eff} = 72{,}000 \pm 2000$ K and $\log g = 5.7 \pm 0.2$ as our best-fit parameters. Scaling the model spectrum to match the star's optical and near-infrared magnitudes, we derive a mass $M_* = 0.53 \pm 0.24\ M_\odot$ and luminosity $\log L/L_\odot = 2.84 \pm 0.05$, consistent with the values expected of an evolved star in a globular cluster. Comparing the star with post-horizontal-branch evolutionary tracks, we conclude that it most likely evolved from the blue horizontal branch, departing the asymptotic giant branch before third dredge-up. It should thus exhibit the abundance pattern (O-poor and Na-rich) characteristic of the second-generation (SG) stars in M4. We derive the star's photospheric abundances of He, C, N, O, Si, S, Ti, Cr, Fe, and Ni. CNO abundances are roughly 0.25 dex greater than those of the cluster's SG stars, while the Si and S abundances match the cluster values. Abundances of the iron-peak elements (except for iron itself) are enhanced by 1–3 dex. Rather than revealing the star's origin and evolution, this pattern reflects the combined effects of diffusive and mechanical processes in the stellar atmosphere.

Key words: stars: abundances – stars: atmospheres – stars: individual (NGC 6121 Y453) – ultraviolet: stars

1. Introduction

The color–magnitude diagrams of Galactic globular clusters frequently include a handful of luminous, blue stars. Called UV-bright stars, these objects are evolving, either from the asymptotic giant branch (AGB) or directly from the extreme horizontal branch (EHB), onto the white-dwarf cooling curve. Their stellar parameters and photospheric abundances thus provide important constraints on theories of low-mass stellar evolution and white-dwarf formation.

First cataloged by Cudworth & Rees (1990), Y453 was identified as a UV-bright star in Ultraviolet Imaging Telescope observations of the globular cluster M4 (NGC 6121; Parise et al. 1995). The star's optical spectrum was studied by Moehler et al. (1998). Fits to its hydrogen and helium lines yielded an effective temperature $T_{\rm eff} = 58{,}800$ K, surface gravity $\log g = 5.15$, and helium abundance $\log N({\rm He})/N({\rm H}) = -0.98$. These parameters place the star on the $0.546\ M_\odot$ post-early AGB evolutionary track of Schönberner (1983), but its derived mass and luminosity ($M_* = 0.16\ M_\odot$ and $\log L/L_\odot = 2.6$) are inconsistent with this evolutionary scenario. To better understand this enigmatic object, we have observed Y453 with the Cosmic Origins Spectrograph (COS) on the *Hubble Space Telescope (HST)*.

Our FUV observations are discussed in Section 2. Section 3 presents a reanalysis of the original optical spectrum. In Section 4, we return to the FUV spectrum, using it to derive the star's effective temperature and photospheric abundances. In Section 5, we discuss the star's cluster membership, derive its mass and luminosity, compare its parameters with new evolutionary models, and compare its abundances with the cluster values. We review our conclusions in Section 6.

2. Observations and Data Reduction

Y453 was observed with *HST*/COS on 2015 February 09 (Program 13721; R. Benjamin, P.I.). A 2048 s exposure, obtained with the G130M grating, extends from 1130 to 1430 Å with a signal-to-noise ratio S/N ∼ 30 per 7 pixel resolution element. A 5603 s exposure, obtained with the G160M grating, extends from 1430 to 1770 Å. Its S/N > 50 at 1430 Å and falls to ∼15 at the longest wavelengths. The flux- and wavelength-calibrated spectra, processed with CALCOS version 3.0, were retrieved from the Mikulski Archive for Space Telescopes (MAST) on 2015 August 28. A link to the data is provided here: [10.17909/T9KC7B].

3. The Optical Spectrum

We begin by returning to the optical spectrum of Y453, which was kindly provided by S. Moehler and is reproduced in Figure 1. Details of the observation, data reduction, and original analysis are presented in Moehler et al. (1998).

We compute a grid of non-local thermodynamic equilibrium (NLTE) stellar atmosphere models using the program TLUSTY (Hubeny & Lanz 1995). The model atmospheres are composed solely of hydrogen and helium. The atomic models for H I, He I, and He II are similar to those that Lanz & Hubeny (2003) used for computing their grid of O-type stars. Our grid of models covers effective temperatures ranging from $T_{\rm eff} = 52{,}000$ to 70,000 K in steps of 2000 K, gravities from $\log g = 5.0$ to 6.0 in steps of 0.2 dex, and He abundance from $\log N({\rm He})/N({\rm H}) = -0.6$ to -2.2 in steps of 0.4 dex. From that grid of model atmospheres, we compute synthetic spectra using the program SYNSPEC (Hubeny 1988). The synthetic spectra are convolved with a Gaussian and normalized to replicate the observed spectrum.

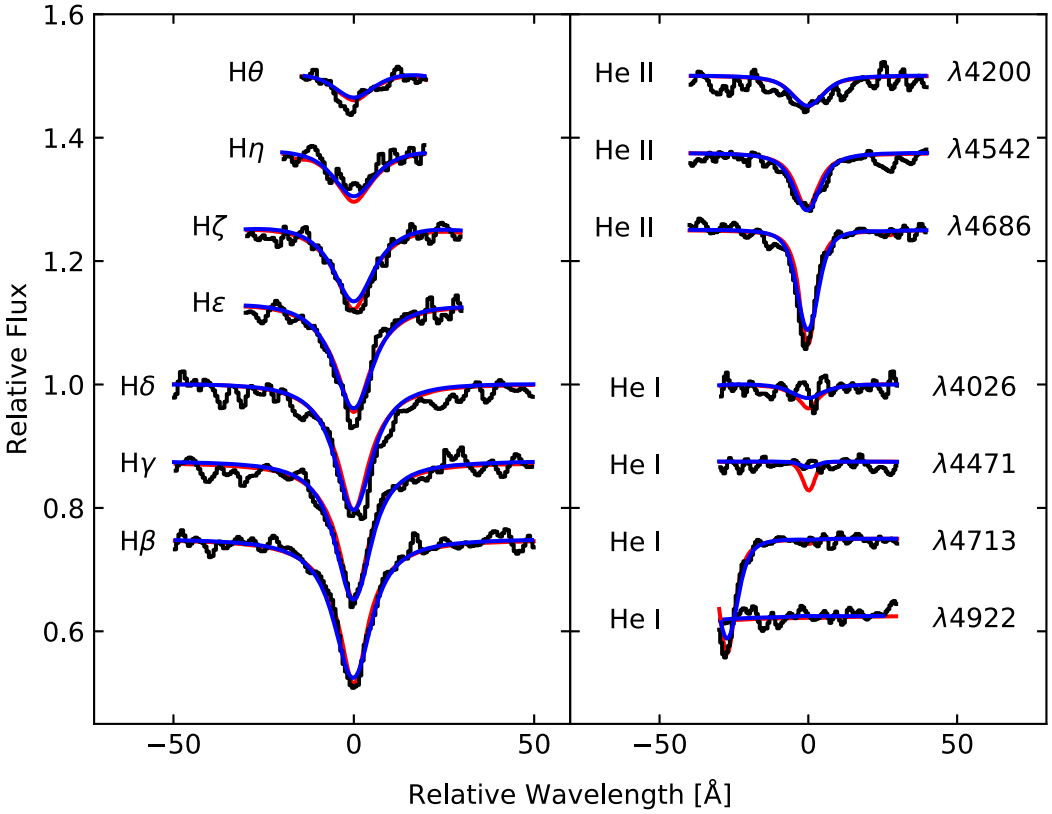

Figure 1. Hydrogen and helium lines in the optical spectrum of Y453 from Moehler et al. (1998) overplotted by our best-fit H+He model (red curve) and best-fit high-metallicity model (10 times solar; blue curve). The He I λ4471 line is not present in the stellar spectrum, but is strong in our H+He models. The line becomes weaker as the model opacity rises.

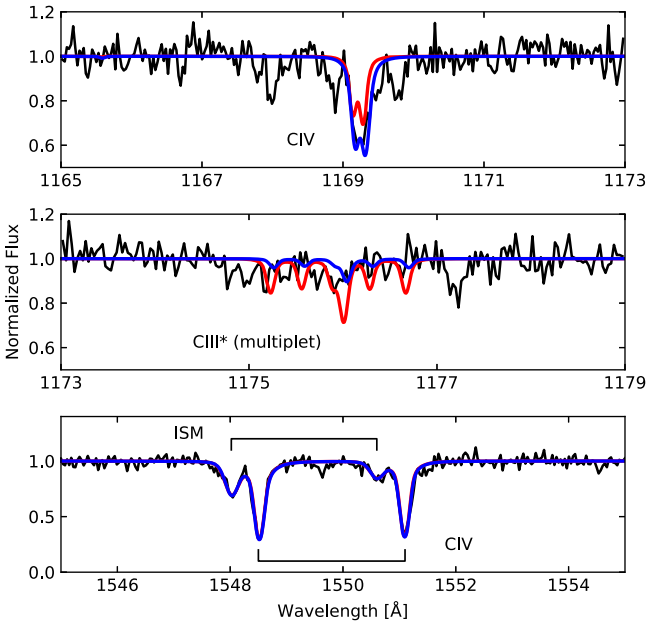

Figure 2. Carbon features in the COS spectrum of Y453. The red curve represents a model with $T_{\rm eff}$ = 56,000 K; the blue curve is 72,000 K. Each model has the best-fit carbon abundance for its temperature. The cooler models overpredict the strength of the C III* multiplet and underpredict the C IV lines at 1169 Å. The interstellar C IV features are modeled with Gaussian absorption lines. For this figure, the data are smoothed by 3 pixels.

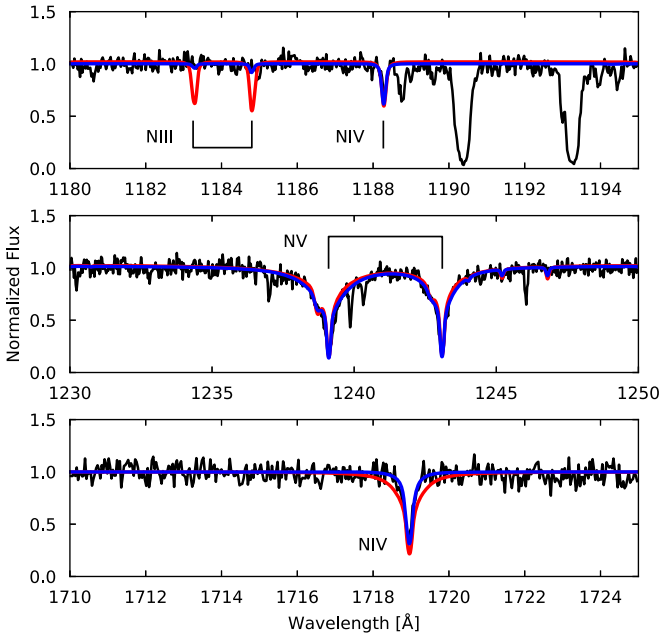

Figure 3. Same as Figure 2, but for nitrogen. The N V lines are blended with ISM features, which we model using the C IV ISM lines as templates. The cooler model overpredicts the strength of the N III lines.

Moehler et al. (1998) reported that the resolution of their spectrum is 6.7 Å, but the cores of the H and He lines are not well fit by models with this resolution. Experimenting with a range of Gaussian line-spread functions, we find that the line cores are best fit by models with a resolution of 4.2 Å. Returning to her observation notes, S. Moehler was able to determine that the detector used in her 1996 observations had

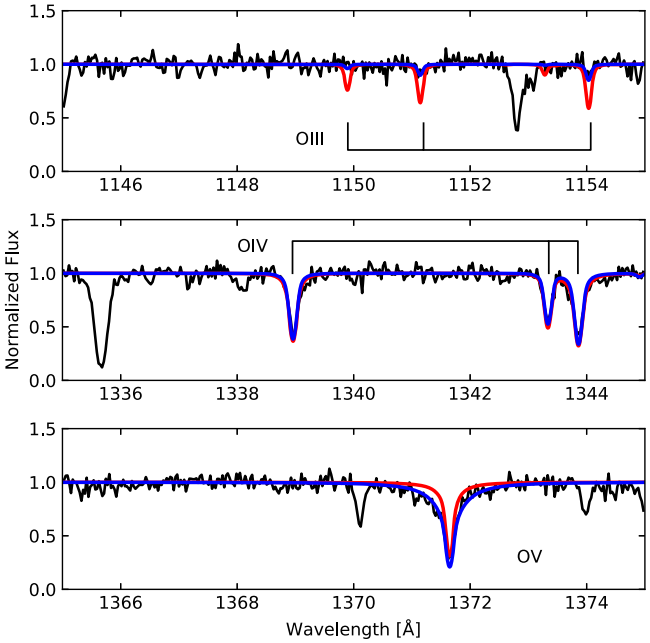

Figure 4. Same as Figure 2, but for oxygen. The cooler model overpredicts the strength of the O III lines.

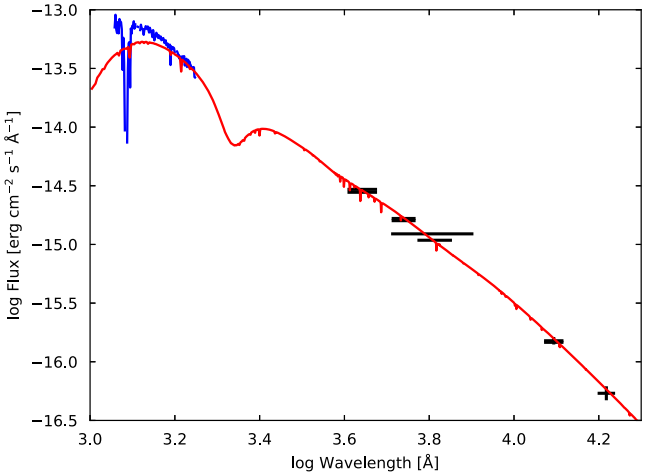

Figure 5. Spectral-energy distribution of Y453. The blue curve is the COS spectrum. Black crosses are optical and NIR magnitudes from the literature, expressed in units of flux. The red curve is our best-fit model; scaled to reproduce the optical and NIR data, it underpredicts the flux at FUV wavelengths. Both the COS and model spectra have been smoothed for this figure.

0.″34 pixels, so a slit width of 1″ should have yielded a spectrum with 5.6 Å resolution. To achieve a resolution of 4.2 Å would have required atmospheric seeing of 0.″8, which is unlikely. We have accordingly adopted a spectral resolution of 5.6 Å in our analysis. With this change, our best-fit stellar parameters are $T_{\rm eff} = 55{,}218 \pm 405$ K, $\log g = 5.60 \pm 0.02$, and $\log N({\rm He})/N({\rm H}) = -1.12 \pm 0.02$.

As we shall see, fits to CNO lines in the star's COS spectrum suggest that $T_{\rm eff} \sim 72{,}000$ K, considerably higher than the temperature derived from its optical spectrum. This discrepancy may be a symptom of the Balmer-line problem (Napiwotzki 1993; Werner 1996), the inability of models to reproduce simultaneously the full set of Balmer lines with a single set of stellar parameters ($T_{\rm eff}$ and $\log g$). Apparently, there are sources of opacity in the atmospheres of hot stars that are not included in our models. An example is the hot subdwarf O star BD +28°4211. According to Napiwotzki (1993), fits to the highest Balmer lines (Hδ or Hϵ) yield $T_{\rm eff} \sim 82{,}000$ K, but fits to the complete Balmer series yield much lower temperatures. Latour et al. (2015) were able to reproduce the higher temperature by fitting the star's complete optical spectrum with a stellar model assuming a metallicity of 10 times solar.

We have extended the Latour et al. (2015) grid of high-metallicity models to cooler temperatures and fit them to the optical spectrum of Y453. Assuming a spectral resolution of 5.6 Å, we derive $T_{\rm eff} = 55{,}870 \pm 780$ K, $\log g = 5.69 \pm 0.04$, and $\log N({\rm He})/N({\rm H}) = -1.08 \pm 0.04$. A similar grid of solar-metallicity models yields $T_{\rm eff} = 54{,}470 \pm 730$ K, $\log g = 5.72 \pm 0.05$, and $\log N({\rm He})/N({\rm H}) = -1.11 \pm 0.04$. (The metallicity of M4 is [Fe/H] = −1.16; Harris 1996, 2010 edition.) In both cases, the spectrum is reasonably well fit. Most interesting is the He I λ4471 line: as shown in Figure 1, the feature is not present in the stellar spectrum, but is strong in our H+He models. It becomes successively fainter as the model metallicity increases, disappearing in the high-metallicity grid. We conclude that high-metallicity models are better able to reproduce the optical spectrum of Y453, but cannot reproduce the high effective temperature derived from the star's FUV spectrum. We adopt the stellar parameters derived from the high-metallicity grid as the best fits to the star's optical spectrum.

4. The FUV Spectrum

4.1. Effective Temperature

Though its optical spectrum is best fit by models with $T_{\rm eff} \sim 56{,}000$ K, the star's COS spectrum requires models with a higher effective temperature. We use simultaneous fits of lines from multiple ionization stages to constrain $T_{\rm eff}$. We begin by fitting the C III and C IV features shown in Figure 2. We construct a grid of models with an atmosphere consisting of H+He+C. The effective temperature ranges from 50,000 to 77,500 K in steps of 2500 K, and the carbon abundance ranges from $\log N({\rm C})/N({\rm H}) = -6.8$ to −3.2 in steps of 0.4 dex. In this grid, the surface gravity is fixed at $\log g = 5.7$ and the helium abundance at $\log N({\rm He})/N({\rm H}) = -1.08$, values derived from the optical spectrum. Models are resampled to the COS pixel scale and convolved with the COS line-spread function. The interstellar C IV doublet at 1550 Å is modeled with a pair of Gaussian absorption features whose relative wavelengths and equivalent widths are fixed at the appropriate ratios. Our best-fit parameters are $T_{\rm eff} = 68{,}876 \pm 1451$ K and $\log N({\rm C})/N({\rm H}) = -4.96 \pm 0.09$. Quoted errors are purely statistical. The carbon lines may underestimate the temperature, because there are many weak Co and Ni features near 1175 Å that could masquerade as C III* lines.

We repeat this process with the N III, N IV, and N V lines shown in Figure 3. The star's N V features are blended with interstellar lines. To account for them, we fit the ISM lines with Gaussians, requiring them to have the same radial velocity (relative to the stellar features) and line width (in units of km s^{-1}) as the interstellar C IV lines. Our best-fit parameters are $T_{\rm eff} = 71{,}383 \pm 1064$ K and $\log N({\rm N})/N({\rm H}) = -3.98 \pm 0.02$. Repeating this process with the O III, O IV, and O V features shown in Figure 4 yields $T_{\rm eff} = 71{,}884 \pm 808$ K and $\log N({\rm O})/N({\rm H}) = -3.79 \pm 0.03$.

Table 1
Abundances from Fits to the COS Spectrum

Species	Lines Fit	Abundance		
		$T_{\rm eff}$ = 72,000 K $\log g$ = 5.7	$T_{\rm eff}$ = 70,000 K $\log g$ = 5.5	Final Value
Carbon	C IV λλ1169, C III* λλ1175, C IV λλ1550	−4.76 ± 0.04	−4.86 ± 0.04	−4.76 ± 0.11
Nitrogen	N III λλ1183, 1185; N IV λ1188; N V λλ1239, 1243; and N IV λ1719	−4.07 ± 0.02	−4.08 ± 0.02	−4.07 ± 0.02
Oxygen	O III λλ1149, 1150, 1153; O IV λλ1338, 1342, 1343; O V λ1371	−3.81 ± 0.03	−3.85 ± 0.03	−3.81 ± 0.05
Silicon	Si IV λλ1394, 1403	−5.02 ± 0.12	−5.09 ± 0.13	−5.02 ± 0.15
Sulfur	S V λ1502	−5.63 ± 0.10	−5.71 ± 0.10	−5.63 ± 0.13
Titanium	Ti V λλ1675, 1687	−5.00 ± 0.36	−5.00 ± 0.37	−5.00 ± 0.36
Chromium	Cr V λλ1490, 1498	−6.99 ± 0.22	−7.06 ± 0.20	−6.99 ± 0.23
Iron	Fe V and Fe VI, 1373–1390 Å	−5.54 ± 0.07	−5.63 ± 0.08	−5.54 ± 0.11
Nickel	Ni V, 1310–1330 Å; Ni VI, 1170–1186 Å	−6.01 ± 0.05	−6.10 ± 0.04	−6.01 ± 0.10

Note. Abundances relative to hydrogen: $\log N(\mathrm{X})/N(\mathrm{H})$. For iron and nickel, we fit multiple absorption features in the listed region(s).

The effective temperatures derived from the nitrogen and oxygen lines agree within their uncertainties. The temperature derived from the carbon lines is lower, but it may suffer from contamination of the C III* multiplet, as mentioned above. Thus, we use only the nitrogen and oxygen results. Their weighted mean is $T_{\rm eff} = 71{,}675 \pm 643$ K. The statistical uncertainties of both the surface gravity and effective temperature are quite small. To better understand the systematic uncertainties of these parameters and their effects on the photospheric abundances (derived below), we follow Rauch et al. (2014) in assuming an uncertainty of 0.2 dex in the surface gravity. Repeating the above analysis assuming $\log g = 5.5$, we derive an effective temperature of $T_{\rm eff} = 70{,}087 \pm 698$ K. We thus adopt as our best-fit parameters $T_{\rm eff} = 72{,}000 \pm 2000$ K and $\log g = 5.7 \pm 0.2$.

4.2. Surface Gravity and Helium Abundance

We would normally derive the surface gravity and helium abundance from simultaneous fits to the hydrogen and helium lines in the UV spectrum, just as we did in the optical, but the star's Lyα line is dominated by interstellar absorption and thus unavailable. The lone helium feature in the COS spectrum is He II λ1640. We fit this line with a two-dimensional grid of NLTE H+He models, allowing both the surface gravity and helium abundance to vary freely. The best-fit values, $\log g \sim 6.8$ and $\log N(\mathrm{He})/N(\mathrm{H}) \sim -1.8$ (exact values depend on the details of the fit), are astrophysically implausible (implying a stellar mass of 6.6 $M_\odot$) and inconsistent with fits to the optical spectrum. We suspect that the same opacity effects that alter the depths of the hydrogen and helium lines at optical wavelengths are at work in the FUV, as well. We will continue to use the optically derived values of the surface gravity and helium abundance.

4.3. Photospheric Abundances

The COS spectrum of Y453 shows absorption from He, C, N, O, Si, S, Ti, Cr, Fe, and Ni. Since oxygen and nitrogen are the most abundant metals in the star's photosphere, we determine their abundances first. To reduce the size of our model grids, we perform the calculation iteratively. Beginning with a grid of models with H+He+O, we determine the oxygen abundance. We then generate a grid with H+He+N+O, holding the oxygen abundance fixed, and determine the nitrogen abundance. Finally, we generate a grid with H+He+N+O, holding the nitrogen abundance fixed, and determine the final oxygen abundance. For all other species, we generate a grid of models with H+He+N+O+X, where N and O are fixed at their best-fit values. All of our models assume that $\log N(\mathrm{He})/N(\mathrm{H}) = -1.08$. Unless otherwise stated, all species are treated in NLTE. We perform the entire analysis twice, first assuming $T_{\rm eff} = 72{,}000$ K and $\log g = 5.7$, then assuming $T_{\rm eff} = 70{,}000$ K and $\log g = 5.5$. The difference in the two results is our estimate of the systematic error in our fits. We add this term and the statistical error in quadrature to compute our final error. Our results are presented in Table 1. Notes regarding individual species follow.

Carbon: Omitting the C IV λλ1550 doublet from the fit does not significantly change the derived carbon abundance.

Nitrogen: While we did not use the line in our fits, we noticed that, in our synthetic spectra, the N III feature at 1730 Å was in emission, while the data show it in absorption. We were using the N III model atom (n3_25+7lev.dat) that Lanz & Hubeny (2003) used to compute their grid of O star models. By adopting a more elaborate model atom (n3_40+9lev.dat), we were able to reproduce the absorption feature at 1730 Å. The new model atom includes several energy levels above the lower energy level of the transition ($E > 330{,}000$ cm^{-1}).

Iron-peak elements: We lack the model atoms necessary to compute full NLTE models for some iron-peak elements, so we use iron, for which we have a complete set of models, to explore NLTE effects in this part of the periodic table. To this end, we generate a second grid of iron spectra, using an NLTE model with a H+He+N+O composition and the LTE approximation to compute the populations of iron in the stellar atmosphere. TLUSTY reports that, in an atmosphere with $T_{\rm eff} = 72{,}000$ K, the dominant ionization state for iron is Fe VI, but the Fe VI lines in our LTE spectra are considerably weaker than those in our NLTE spectra. Fitting our LTE models to the Fe V lines in this bandpass yields $\log N(\mathrm{Fe})/N(\mathrm{H}) = -5.58 \pm 0.07$, a value consistent with that derived from the NLTE models. Fitting the same models to the Fe VI lines (principally Fe VI λ1374.6) yields $\log N(\mathrm{Fe})/N(\mathrm{H}) = -5.12 \pm 0.13$, an overestimate of roughly 0.4 dex. Cr V, Fe V, and Ni V have ionization energies of 69, 75, and 76 eV,

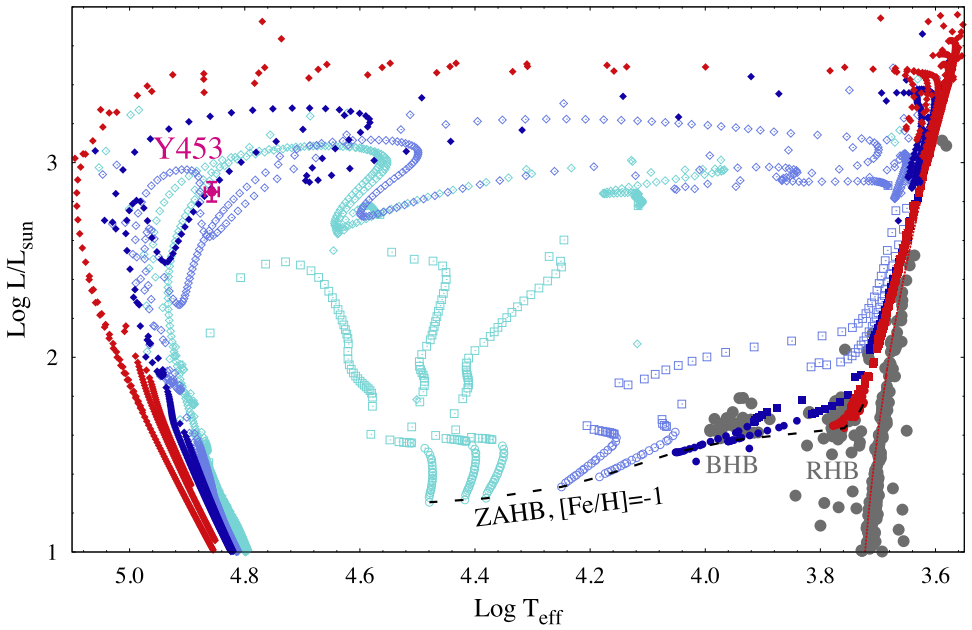

Figure 6. Evolutionary tracks for stars similar to those of M4 during and after the horizontal-branch stage. Colors indicate stars that spend their core helium-burning stage on the RHB (red), BHB (blue), and EHB (cyan). Circles are plotted every 10 Myr, squares are plotted every 1 Myr, and diamonds indicate intervals of 20,000 years. Tracks with ZAHB temperatures greater than those of the HB stars in M4 are indicated by open symbols. Gray points are stars in M4. Y453 is indicated by the solid pink circle.

respectively, so we would expect their populations to vary similarly with temperature. Ti V is not such a good match: its ionization energy is 99 eV, equal to the value for Fe VI. If Ti V behaves like Fe VI, then the titanium abundance derived from Ti V lines may be overestimated by ∼0.4 dex.

Titanium and Chromium: For these species, we lack the model atoms necessary to construct a full NLTE model atmosphere. Instead, we generate an LTE grid of models, just as we did for iron. We fit only the lines of Ti V and Cr V when computing LTE abundances.

Nickel: We have model atoms for ionization states Ni I through Ni VI, but lack a model for Ni VII. While Ni VI is the dominant ionization state in the line-forming region of the stellar atmosphere, omitting Ni VII from our models will cause us to overpredict the populations of the lower ionization states. To examine the effect of the missing Ni VII ions, we generate an LTE grid of models, just as we did for iron. Fitting only the Ni V features, we derive an abundance $\log N(\mathrm{Ni})/N(\mathrm{H}) = -5.93 \pm 0.05$, a result consistent with that derived from the NLTE models.

An important systematic uncertainty in our fits is the placement of the stellar continuum. Our models are incomplete; specifically, our line lists lack many weak absorption features. To address this shortcoming, we often set the model continuum slightly higher than the mean level of the observed spectrum. The idea is that, when the S/N is high, small dips in the spectrum are not noise features, but weak absorption lines not included in the model. When the S/N is low, these dips are just noise. As an experiment, we scale the model by a factor of 1.03 relative to the normalized spectrum. A higher continuum requires deeper absorption features—and thus higher abundances—to reproduce the spectrum. For the iron-peak elements, the best-fit abundances rise by an average of 0.4 dex. None of the fits reported in Table 1 employ a rescaled continuum.

5. Discussion

5.1. Cluster Membership

Our analysis is predicated on the assumption that Y453 is a member of M4. Before proceeding, we should confirm that this assumption is correct. The average heliocentric radial velocity of the cluster is $\langle v \rangle = +71.08 \pm 0.08\ \mathrm{km\ s^{-1}}$, with a dispersion of $3.97\ \mathrm{km\ s^{-1}}$ (Malavolta et al. 2015). A comparison of the stellar and interstellar features in our COS spectrum yields a heliocentric radial velocity of $+69\ \mathrm{km\ s^{-1}}$ for Y453 (B. Wakker 2016, private communication), a value within 1σ of the cluster mean. From proper-motion measurements, Cudworth & Rees (1990) derive a cluster membership probability of 99% for Y453. We conclude that Y453 is a cluster member.

5.2. Stellar Mass and Luminosity

We can derive the star's radius, and from this its mass and luminosity, by comparing its observed and predicted flux. Any such comparison must take into account dust extinction along the line of sight. M4 is the globular cluster nearest the Sun, yet its extinction is both high and highly variable, owing to its location in the Galactic plane, behind the Sco-Oph cloud complex. Hendricks et al. (2012) used a combination of broadband near-infrared (NIR) and optical Johnson-Cousins photometry (specifically, the B, V, I, J, and K_s bands) to study the dust along this line of sight. They found that the reddening to M4 is well modeled by the extinction curve of Cardelli et al. (1989, hereafter CCM). Using this parameterization, they derive a dust-type parameter $R_V = 3.62 \pm 0.07$, a value considerably higher than the $R_V = 3.1$ commonly assumed for the diffuse ISM. Across the cluster (roughly $10' \times 10'$), the total range in reddening is about 0.2 mag; the mean extinction is $E(B-V) = 0.37 \pm 0.01$.

The spectral irradiance of Y453 has been measured in a range of optical and NIR bands: $B = 15.914 \pm 0.005$, $V = 15.857 \pm 0.003$ (Mochejska et al. 2002); $B = 15.852 \pm 0.003$,

$V = 15.904 \pm 0.009$, $R_C = 15.792 \pm 0.007$, $J = 15.635 \pm 0.013$ (Libralato et al. 2014); $J = 15.601 \pm 0.080$, $H = 15.774 \pm 0.149$ from 2MASS (Skrutskie et al. 2006); and $G = 15.784 \pm 0.002$ from *Gaia* Data Release 1 (Brown & Gaia Collaboration 2016).

To model the stellar continuum, we employ an NLTE model with $T_{\rm eff} = 72{,}000$ K, $\log g = 5.7$, $\log N({\rm He})/N({\rm H}) = -1.08$, and the CNO abundances derived in Section 4.3. Synthetic stellar magnitudes are computed using the Python package Pysynphot (Lim et al. 2015). We compute magnitudes relative to the spectrum of Vega, adjusting the zero points of the B, V, and R_C filters as described in Appendix B of Lim et al., but using the V-band correction of Bohlin (2007). We assume that the zero point for the *Gaia* G band is the same as for the V band, and we take as the zero points for the J and H bands the observed magnitudes of Vega as reported by 2MASS. We adopt the dust model of Hendricks et al. (2012) and employ a χ^2 minimization algorithm. Free parameters in the fit are the scale factor of the model continuum and the extinction parameter $E(B-V)$. The best-fit model, with a scale factor $\phi = (5.56 \pm 0.05) \times 10^{-23}$ and an extinction $E(B-V) = 0.349 \pm 0.002$, is plotted in Figure 5.

In the synthetic spectra generated by SYNSPEC, the flux is expressed in terms of the flux moment, H_λ. If the star's radius and distance are known, then the scale factor required to convert the model to the flux at earth is $\phi = 4\pi(R_*/d)^2$ (Kurucz 1979). Using the distance $d = 1.82 \pm 0.04$ kpc derived from measurements of three eclipsing binaries in M4 (Kaluzny et al. 2013), we solve for the stellar radius $R_* = 0.170 \pm 0.004\ R_\odot$. Adopting this value and our best-fit surface gravity ($\log g = 5.7 \pm 0.2$), we derive a stellar mass $M_* = 0.53 \pm 0.24\ M_\odot$. Finally, combining the stellar radius with our best-fit effective temperature ($T_{\rm eff} = 72{,}000 \pm 2000$ K), we derive a stellar luminosity $\log L/L_\odot = 2.84 \pm 0.05$.

From a spectroscopic analysis of 10 white dwarfs in M4, Kalirai et al. (2009) found that the mean mass of stars at the tip of the white-dwarf cooling sequence is $0.53 \pm 0.01\ M_\odot$. If Y453 has evolved past the horizontal branch, as is certainly the case, then it should have a core mass of $0.53\ M_\odot$ and a total mass that is not much greater. The derived mass of Y453, $M_* = 0.53 \pm 0.24\ M_\odot$, is thus precisely what we would expect of an evolved star in M4. The exact agreement of the predicted and derived masses is fortuitous, given the 50% uncertainty in the derived value, but it is a useful check on the star's surface gravity. The derived mass scales with the surface gravity (not its logarithm), and thus is exquisitely sensitive to the adopted value of $\log g$.

Recall that our value of the surface gravity, $\log g = 5.7$, was obtained by fitting high-metallicity models to the optical spectrum of Y453. Had they used similar models, Moehler et al. (1998) would have derived a stellar mass similar to ours, even with their lower effective temperature. They wrote, "In order to obtain a mass of $0.55\ M_\odot$, the value of $\log g$ would need to be 5.68 instead of 5.15."

In Figure 5, the red curve represents the model, and black crosses indicate the optical and NIR magnitudes. Though the model is scaled to fit only the optical and NIR data, we extend it into the FUV for comparison to the COS spectrum, which is plotted in blue. The Hendricks et al. (2012) reddening law for the line of sight to M4 successfully reproduces the observed optical and NIR measurements, but it overpredicts the extinction in the FUV. Attempts to fit both the COS and optical/NIR data with a single CCM extinction curve have been unsuccessful. Note that the model spectrum shows no significant Lyα absorption; the strong line seen in the COS spectrum is interstellar.

5.3. Evolutionary Status

To better understand the evolutionary state of Y453, we compare it to post-HB evolutionary tracks for stars similar to those in M4. These tracks, shown in Figure 6, represent an extension of the work presented by Miller Bertolami (2016). The models are computed for [Fe/H] $= -1.0$ and a zero-age main-sequence (ZAMS) mass of $M_{\rm ZAMS} = 0.85\ M_\odot$, assuming a scaled-solar metal content with initial abundances $Z_{\rm ZAMS} = 0.00172$, $Y_{\rm ZAMS} = 0.24844$, and $X_{\rm ZAMS} = 0.74984$. The models evolve naturally from the ZAMS, except on the RGB, where we impose a range of mass-loss rates to ensure the population of the extreme, blue, and red horizontal branches (EHB, BHB, and RHB, respectively). Zero-age horizontal-branch (ZAHB) masses are $M_{\rm ZAHB} = 0.85$, 0.75, 0.70, and $0.65\ M_\odot$ (final masses $M_{\rm WD} = 0.555$, 0.545, 0.537, and $0.528\ M_\odot$) for the RHB (red points); $M_{\rm ZAHB} = 0.60$, 0.58, 0.55, and $0.53\ M_\odot$ (final masses $M_{\rm WD} = 0.518$, 0.513, 0.504, and $0.499\ M_\odot$) for the BHB (blue points); and $M_{\rm ZAHB} = 0.50$, 0.495, and $0.49\ M_\odot$ (final masses $M_{\rm WD} = 0.496$, 0.495, and $0.49\ M_\odot$) for the EHB (cyan points).

To these evolutionary tracks, we have added a sample of M4 stars from the photometry of Mochejska et al. (2002). Marino et al. (2011) and Villanova et al. (2012) computed effective temperatures for about two dozen stars that span the HB of M4; we use their results to derive a relation between observed $B-V$ and $T_{\rm eff}$. Malavolta et al. (2014) derived effective temperatures for 2191 stars in M4, but deliberately excluded the HB. We employ their technique to derive $T_{\rm eff}$ for the cluster's giant stars. Luminosities are computed from V magnitudes assuming the cluster parameters of Hendricks et al. (2012) and the bolometric corrections given by Cox (2000). For the purpose of this figure, differential reddening across the cluster is ignored.

With $\log T_{\rm eff} = 4.86$ and $\log L/L_\odot = 2.84$, Y453 occupies a region of parameter space shared by post-EHB stars that evolve directly from the horizontal branch (cyan points) and post-BHB stars that evolve at least partway up the AGB (blue points). We can reject an EHB origin for Y453, because M4 does not possess an EHB (ZAHB stars with $T_{\rm eff} \geqslant 22{,}000$ K). As shown in Figure 6, the cluster has a bimodal horizontal branch, well populated on both sides of the RR-Lyrae gap, but its BHB stars have temperatures $T_{\rm eff} \lesssim 10{,}000$ K (Marino et al. 2011; Villanova et al. 2012). We conclude that Y453 is a post-BHB star. Its low carbon abundance ($N_C/N_O = 0.11$) indicates that the star left the AGB before third dredge-up.

Villanova et al. (2012) found evidence that the BHB stars in M4 are enriched in helium. Could their higher helium abundance alter their subsequent evolution? In fact, the helium enhancement is only about $\Delta Y = 0.02$ relative to the RHB, an amount will not significantly affect the BHB stars or their post-BHB evolution. In the core helium-burning stage, other uncertainties, among them the size of the convective core, will dominate.

5.4. Photospheric Abundances

Galactic globular clusters host multiple stellar populations. First-generation (FG) stars display abundances typical of halo

Table 2
Photospheric Abundances of Y453, M4, and the Sun

Species	Y453	M4 RGB		M4 HB		Sun
		FG	SG	FG/RHB	SG/BHB	
Helium	−1.08 ± 0.04	···	···	···	−0.99 ± 0.02	−1.07 ± 0.01
Carbon	−4.76 ± 0.10	−4.85 ± 0.02	−5.01 ± 0.02	···	···	−3.57 ± 0.05
Nitrogen	−4.07 ± 0.02	−5.03 ± 0.03	−4.39 ± 0.02	···	···	−4.17 ± 0.05
Oxygen	−3.81 ± 0.04	−3.89 ± 0.03	−4.06 ± 0.03	−3.79 ± 0.01	−4.02 ± 0.02	−3.31 ± 0.05
Sodium	···	−6.83 ± 0.02	−6.42 ± 0.02	−6.81 ± 0.03	−6.46 ± 0.02	−5.76 ± 0.04
Silicon	−5.02 ± 0.12	−5.10 ± 0.02	−5.11 ± 0.02	···	···	−4.49 ± 0.03
Sulfur	−5.63 ± 0.13	−5.54 ± 0.03	−5.54 ± 0.03	···	···	−4.88 ± 0.03
Titanium	−5.00 ± 0.36	−7.85 ± 0.02	−7.89 ± 0.01	···	···	−7.05 ± 0.05
Chromium	−6.99 ± 0.23	−7.51 ± 0.02	−7.50 ± 0.03	···	···	−6.36 ± 0.04
Iron	−5.54 ± 0.11	−5.64 ± 0.01	−5.64 ± 0.02	−5.64 ± 0.02	−5.57 ± 0.02	−4.50 ± 0.04
Nickel	−6.01 ± 0.10	−6.88 ± 0.01	−6.90 ± 0.01	···	···	−5.78 ± 0.04

Note. Abundances relative to hydrogen: log $N(X)/N(H)$. M4 RGB values from Villanova & Geisler (2011); sulfur values from Kacharov et al. (2015). M4 HB values from Marino et al. (2011); helium value from Villanova et al. (2012). Solar values from Asplund et al. (2009). FG—first generation; SG—second generation.

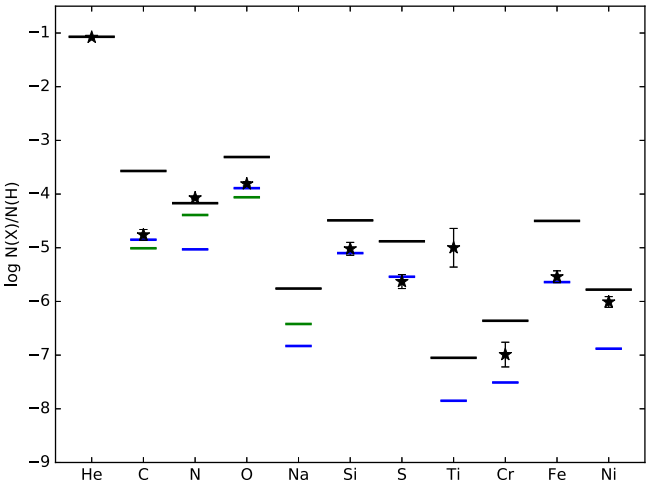

Figure 7. Photospheric abundances of Y453 (stars), the RGB stars in M4 (blue and green lines), and the Sun (black lines). Second-generation RGB stars (green lines) are enhanced in N and Na, and depleted in C and O, relative to first-generation RGB stars (blue lines). The two generations have identical abundances of elements heavier than Na.

field stars, while second-generation (SG) stars, which may have multiple subpopulations, differ in their abundance of elements affected by proton-capture reactions (e.g., C, N, O, Na). Models suggest that the second generation formed from gas polluted by material expelled by massive stars of the first generation. (For details, see the review by Gratton et al. 2012.) Among RGB stars in M4, SG stars are enhanced in N and Na and depleted in C and O relative to first-generation stars (Villanova & Geisler 2011). The two populations exhibit the same abundances of α (Mg, Si, S, Ca, Ti) and iron-peak (Cr, Fe, Ni) elements. The Li and Al abundances and the total C+N+O content are also the same. Table 2 and Figure 7 present the measured abundances of Y453, various subpopulations of M4 (Marino et al. 2011; Villanova & Geisler 2011; Villanova et al. 2012; Kacharov et al. 2015), and the Sun (Asplund et al. 2009).

Marino et al. (2011) found a correlation between the abundances and colors of stars on the HB of M4. RHB stars exhibit the abundance pattern (O-rich and Na-poor) characteristic of FG stars, while BHB stars exhibit the pattern (O-poor and Na-rich) characteristic of SG stars (Table 2). Villanova et al. (2012) reported that BHB stars are enriched in He, as would be expected of SG stars. We have concluded that Y453 is a post-BHB star that did not experience third dredge-up, and thus would expect its abundances to match those of the cluster's SG stars.

In Figure 7, we see that the CNO abundances of Y453 are 0.25 dex greater than those of the SG RGB stars, while the Si and S abundances match those of the cluster. Of the iron-peak elements, only iron itself matches the cluster abundance. In particular, Ti is overabundant by roughly three orders of magnitude. As discussed in Section 4.3, we lack model atoms for Ti, Cr, and the Ni VII ion, but these shortcomings should not result in such large abundance errors. We are comparing the abundances of a $T_{\rm eff} = 72{,}000$ K subdwarf O star derived using NLTE models of FUV lines with those of $T_{\rm eff} = 5000$ K RGB stars derived using LTE models of optical lines (some of them molecular), so systematic differences in the models, the atomic parameters, and the line-formation mechanisms cannot be ignored; however, they are probably not driving the observed discrepancy. For example, the non-LTE abundance corrections for C, N, O, Na, and Si should be negligible, while those for S and the iron-peak elements are of the order of 0.1 dex (Asplund 2005).

The high luminosity and surface gravity of Y453 suggest that diffusion processes such as gravitational settling are at work in its atmosphere. To examine this possibility, we have carried out time-dependent diffusion calculations of C, N, O, Si, S, and Fe for two sdO model atmospheres with $\log T_{\rm eff} = 4.84$ and $\log g = 5.6$ and 5.8, respectively. The initial abundances are homogeneous and correspond to the star's observed abundances. Figure 8 shows the evolution of the oxygen abundance as a function of time for the $\log g = 5.6$ model. At the stellar surface, the oxygen abundance decreases by about six orders of magnitude in less than 10,000 years. For the $\log g = 5.8$ model, the abundance falls even more quickly. For all species, the abundance drops below $\log N(X)/N(H) = -10$ in about 10,000 years. From our evolutionary tracks, we estimate that the atmospheric parameters of Y453 have changed little in the past 50,000 years (Figure 6), providing ample time for its photosphere to be stripped of metals. The fact that we detect any metals, let alone enhancements, suggests that other processes are working to maintain the elements heavier than hydrogen in the atmosphere of the star.

One possibility is that the star's abundances are elevated via radiative levitation. Fontaine et al. (2008) were able to reproduce

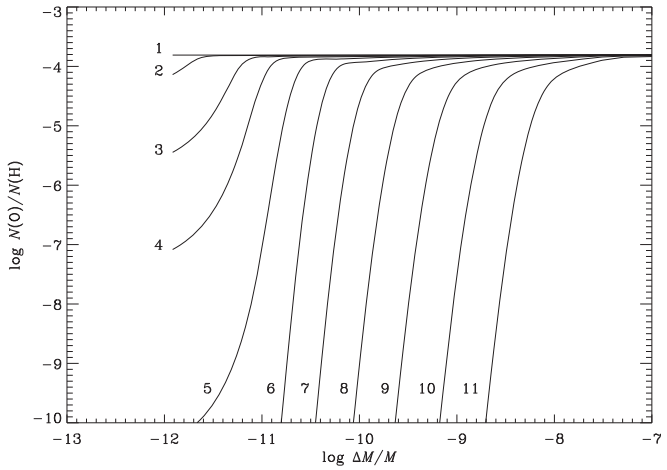

Figure 8. Oxygen abundance profiles in a model atmosphere with log $T_{\rm eff} = 4.86$ and $\log g = 5.6$ at 11 time steps. The numbers next to the abundance profiles indicate the time: (1) 0 years, (2) 500 years, (3) 2500 years, (4) 5000 years, (5) 10,000 years, (6) 20,000 years, (7) 40,000 years, (8) 80,000 years, (9) 160,000 years, (10) 320,000 years, and (11) 640,000 years. The surface of the star is on the left-hand side of the figure. The surface oxygen abundance decreases by about 6 orders of magnitude in less than 10,000 years.

the pulsations observed in the hot sdO star SDSS J160043.6+074802.9 ($T_{\rm eff} = 71{,}070 \pm 2725$ K, $\log g = 5.93 \pm 0.11$, and $\log N({\rm He})/N({\rm H}) = -0.85 \pm 0.08$) by including radiative levitation of iron in their atmospheric model. (A Fourier analysis of the time-tagged COS data for Y453 reveals no evidence of periodic luminosity variations.) Ringat & Rauch (2012) reproduced the general shape of the FUV spectrum of the sdO star EC 11481-2303 ($T_{\rm eff} = 55{,}000$ K, $\log g = 5.8$, and $\log N({\rm He})/N({\rm H}) = -2.6$) using a radiative-transport code that models diffusion processes, including radiative levitation. Their best-fit model predicts extreme super-solar abundances for iron and nickel, suggesting that levitation is particularly efficient in that star. The atmospheric parameters of both stars are similar to those of Y453, so radiative levitation may be at work here, as well.

Another possibility is that a weak stellar wind strips away the outer layers of the star more quickly than gravitational settling can deplete their metals. Figure 8 shows that, after 50,000 years, gravitational settling affects the outer 10^{-9} of the stellar mass. At lower depths, the abundances are essentially unchanged. To lose $\Delta M = 5 \times 10^{-10}\ M_\odot$ via winds in 50,000 years would require a mass-loss rate of $10^{-14}\ M_\odot\ {\rm yr}^{-1}$. There is no evidence of a stellar wind in the spectrum of Y453, but we can set a rough limit on its mass-loss rate. A COS spectrum of the UV-bright star vZ 1128 in M3 exhibits P Cygni profiles in a single absorption feature, the N V $\lambda\lambda$1239, 1243 doublet (Chayer et al. 2015). Model fits to this profile suggest that the wind has a terminal velocity $v_\infty = 380$ km s^{-1} and mass-loss rate $\dot{M} = 10^{-10}\ M_\odot\ {\rm yr}^{-1}$. For simplicity, we fit the N V doublet of Y453 using the same wind model used to fit vZ 1128, varying only the mass-loss rate, which we hold constant as a function of velocity. Since our goal is an upper limit on $\dot{M}$, we do not include the ISM features in our model; this choice has little effect, as the wind profile is dominated by material at higher velocities. We set a 3σ upper limit of $\dot{M}q = 1.4 \times 10^{-14}\ M_\odot\ {\rm yr}^{-1}$, where q represents the fraction of nitrogen in the form of N^{+4}. TLUSTY predicts that $q \sim 0.8$, so $\dot{M} < 1.75 \times 10^{-14}\ M_\odot\ {\rm yr}^{-1}$. We cannot exclude the possibility that a weak stellar wind is responsible for maintaining the metal abundances seen in the stellar photosphere.

Because gravitational settling would quickly remove all metals from the photosphere, other effects must be at work. While we cannot quantify their contributions, they are likely to include radiative levitation, a weak stellar wind, and perhaps atmospheric turbulence.

6. Conclusions

We have performed a spectral analysis of the UV-bright star Y453 in M4. Fits to the star's optical spectrum with metal-enriched model atmospheres yield $T_{\rm eff} = 55{,}870 \pm 780$ K and $\log g = 5.69 \pm 0.04$. Fits to the star's COS spectrum reveal it to have an effective temperature $T_{\rm eff} = 71{,}675 \pm 643$ K, considerably greater than the optically derived value. We adopt $T_{\rm eff} = 72{,}000 \pm 2000$ K, $\log g = 5.7 \pm 0.2$ as our best-fit atmospheric parameters. We scale the model to match the star's optical and near-infrared magnitudes and derive a stellar mass and luminosity that are consistent with the values expected of an evolved star in M4. We conclude that the star evolved from the blue horizontal branch, departing the AGB before third dredge-up. It should thus exhibit the abundance pattern (O-poor and Na-rich) characteristic of SG stars. Instead, we find that its CNO abundances are roughly 0.25 dex greater than those of the cluster's SG stars, while the Si and S abundances match those of the cluster. Abundances of the iron-peak elements (except for iron itself) are enhanced by 1–3 dex. It is likely that the observed abundances of Y453 represent the combined effects of multiple diffusion and mechanical processes within the stellar photosphere.

While we have resolved the mysteries highlighted by Moehler et al. (1998)—the astrophysically implausible values of the star's mass and luminosity—we have identified one more. We are unable to resolve the discrepancy between the effective temperatures derived from the star's optical and FUV spectra. Doing so is likely to require additional optical data with greater resolution and higher signal-to-noise.

The authors wish to thank S. Moehler for generously providing her optical spectrum of Y453 and for extensive conversations about its analysis. We thank B. Wakker for his analysis of the radial velocity of Y453 and the ISM features in its spectrum. This work was supported by NASA grant *HST*-GO-13721.001-A to the University of Wisconsin, Whitewater. P.C. is supported by the Canadian Space Agency under a contract with NRC Herzberg Astronomy and Astrophysics. M.L. acknowledges support from the Alexander von Humboldt Foundation. M.M.M.B. is partially supported by ANPCyT through grant PICT-2014-2708, by the MinCyT-DAAD bilateral cooperation program through grant DA/16/07, and by a Return Fellowship from the Alexander von Humboldt Foundation. This work has made use of NASA's Astrophysics Data System Bibliographic Services (ADS) and the Mikulski Archive for Space Telescopes (MAST), hosted at the Space Telescope Science Institute. STScI is operated by the Association of Universities for Research in Astronomy, Inc., under NASA contract NAS5-26555. This work has made use of data products from the Two Micron All Sky Survey, which is a joint project of the University of Massachusetts and the Infrared Processing and Analysis Center/California Institute of Technology, funded by the National Aeronautics and Space Administration and the National Science Foundation. This work has made use of data from the European Space Agency (ESA) mission *Gaia*,[5]

[5] http://www.cosmos.esa.int/gaia

processed by the *Gaia* Data Processing and Analysis Consortium (DPAC).[6] Funding for the DPAC has been provided by national institutions, in particular, the institutions participating in the *Gaia* Multilateral Agreement.

Facility: HST(COS).

Software: CALCOS (v3.0), TLUSTY (Hubeny & Lanz 1995), SYNSPEC (Hubeny 1988), Pysynphot (Lim et al. 2015).

ORCID iDs

William V. Dixon https://orcid.org/0000-0001-9184-4716

References

Asplund, M. 2005, ARA&A, 43, 481
Asplund, M., Grevesse, N., Sauval, A. J., & Scott, P. 2009, ARA&A, 47, 481
Bohlin, R. C. 2007, in ASP Conf. Ser. 364, The Future of Photometric, Spectrophotometric and Polarimetric Standardization, ed. C. Sterken (San Francisco, CA: ASP), 315
Brown, A. G. A. & Gaia Collaboration 2016, A&A, 595, A2
Cardelli, J. A., Clayton, G. C., & Mathis, J. S. 1989, ApJ, 345, 245
Chayer, P., Dixon, W. V., Fullerton, A. W., Ooghe-Tabanou, B., & Reid, I. N. 2015, MNRAS, 452, 2292
Cox, A. N. 2000, Allen's Astrophysical Quantities (4th ed.; New York: AIP Press; Springer), 388
Cudworth, K. M., & Rees, R. 1990, AJ, 99, 1491
Fontaine, G., Brassard, P., Green, E. M., et al. 2008, A&A, 486, L39
Gratton, R. G., Carretta, E., & Bragaglia, A. 2012, A&ARv, 20, 50
Harris, W. E. 1996, AJ, 112, 1487
Hendricks, B., Stetson, P. B., VandenBerg, D. A., & Dall'Ora, M. 2012, AJ, 144, 25
Hubeny, I. 1988, CoPhC, 52, 103
Hubeny, I., & Lanz, T. 1995, ApJ, 439, 875
Kacharov, N., Koch, A., Caffau, E., & Sbordone, L. 2015, A&A, 577, A18
Kalirai, J. S., Saul Davis, D., Richer, H. B., et al. 2009, ApJ, 705, 408
Kaluzny, J., Thompson, I. B., Rozyczka, M., et al. 2013, AJ, 145, 43
Kurucz, R. L. 1979, ApJS, 40, 1
Lanz, T., & Hubeny, I. 2003, ApJS, 146, 417
Latour, M., Fontaine, G., Green, E. M., & Brassard, P. 2015, A&A, 579, A39
Libralato, M., Bellini, A., Bedin, L. R., et al. 2014, A&A, 563, A80
Lim, P. L., Diaz, R. I., & Laidler, V. 2015, PySynphot User's Guide (Baltimore: STScI)
Malavolta, L., Piotto, G., Bedin, L. R., et al. 2015, MNRAS, 454, 2621
Malavolta, L., Sneden, C., Piotto, G., et al. 2014, AJ, 147, 25
Marino, A. F., Villanova, S., Milone, A. P., et al. 2011, ApJ, 730, L16
Miller Bertolami, M. M. 2016, A&A, 588, A25
Mochejska, B. J., Kaluzny, J., Thompson, I., & Pych, W. 2002, AJ, 124 1486
Moehler, S., Landsman, W., & Napiwotzki, R. 1998, A&A, 335, 510
Napiwotzki, R. 1993, AcA, 43, 343
Parise, R., Stecher, T. P. & UIT Team 1995, BAAS, 27, 836
Rauch, T., Rudkowski, A., Kampka, D., et al. 2014, A&A, 566, A3
Ringat, E., & Rauch, T. 2012, in ASP Conf. Ser. 452, Fifth Meeting on Hot Subdwarf Stars and Related Objects, ed. D. Kilkenny, C. S. Jeffery, & C. Koen (San Francisco, CA: ASP), 71
Schönberner, D. 1983, ApJ, 272, 708
Skrutskie, M. F., Cutri, R. M., Stiening, R., et al. 2006, AJ, 131, 1163
Villanova, S., & Geisler, D. 2011, A&A, 535, A31
Villanova, S., Geisler, D., Piotto, G., & Gratton, R. G. 2012, ApJ, 748, 62
Werner, K. 1996, ApJL, 457, L39

[6] http://www.cosmos.esa.int/web/gaia/dpac/consortium